Pre-oxidation of porous ferritic Fe22Cr alloys for lifespan extension at high-temperature

D. Koszelow [a,*], M. Makowska [b], F. Marone [c], G. Cempura [d], M. Tomas [e], J. Froitzheim [e], S. Molin [a]

[a] Advanced Materials Centre, Faculty of Electronics, Telecommunications and Informatics, Gdańsk University of Technology, Gdańsk 80-233, Poland
[b] Laboratory of Nuclear Materials, Laboratory of Synchrotron Radiation and Femtochemistry, Paul Scherrer Institut, Villigen 5232, Switzerland
[c] Swiss Light Source, Paul Scherrer Institut, Villigen, Switzerland
[d] Centre of Electron Microscopy for Materials Science, Faculty of Metal Engineering and Industrial Computer Science, AGH University of Krakow, Al. Mickiewicza 30, Krakow 30-059, Poland
[e] Energy and Materials, Chalmers University of Technology, Kemivägen 10, Gothenburg 41296, Sweden

ABSTRACT

Pre-oxidation of porous ferritic Fe22Cr alloys was extensively studied in this paper. Weight gain measurements and SEM analysis revealed that pre-oxidation performed at 900°C for 40 min increased the lifespan of the alloy. A Cr evaporation study did not disclose any significant influence of the pre-oxidation process on the Cr content in the alloy. For a more detailed assessment, TEM imaging and X-ray tomography measurements of pre-oxidized samples were performed. These analyses showed that alteration in the grain and grain boundary diffusion fluxes might be the key for explaining the corrosion prevention role of pre-oxidation.

1. Introduction

Advanced alloys are essential for high-temperature devices, including gas turbines, engines, and heat exchangers [1–3]. In recent years, ferritic high-chromium alloys have been considered as support materials for solid oxide cells (SOCs) [4–9]. Advanced ceramic components, which are widely used in SOCs, are expensive and difficult to manufacture [10]. Thus, the application of alloys allows for decreasing the cost of the device and provides shape flexibility.

The typical operating temperature of SOCs exceeds 600°C [11], thus the basic hindrance to using metallic components is the corrosion process [12]. The oxide scale, which is the result of the corrosion process, limits the lifespan of the whole device by decreasing the electrical conductivity of the metallic support. Alloys protection from high-temperature corrosion relies upon the formation of a passivating, protective layer on their surface that limits further oxide growth. [13–15].

One of the elements that forms the passivating layer of oxide scale on the alloy surface in typical SOC operating conditions is chromium. Chromia (Cr_2O_3) has a reasonably high conductivity ($\sim 1 - 10$ mS cm^{-1} at $600\,°C - 800\,°C$ [16]) combined with low oxide scale growth. Cr-based ferritic alloys like Crofer 22 APU or Crofer 22 H are considered a support material in solid oxide cells [17]. [18–21]. For alloys that contain more than 26 wt% of Cr, the brittle sigma phase occurs at high temperatures, which is not desirable in the context of solid oxide cell application [22].

The corrosion process has been described in detail throughout the last decades for dense alloys [23–25]. Nevertheless, there are only a limited number of publications about the corrosion of porous ferritic alloys, especially in the context of their lifetime in solid oxide cell operating conditions [26–32]. Koszelow et al. showed that for the same chemical composition and thickness of the alloy sheet, the specific surface area of a porous alloy ($\sim$30% porosity) can be 28 times higher than that of a dense form [30]. It indicates a higher contact area between the alloy surface and air, which is a key factor in defining the oxide scale growth rate process.

There are several approaches to evaluate the threshold value of the alloy's lifespan. Tucker et al. defined a threshold value for the oxide scale thickness ($\sim$3 μm), which determines the lifespan of the porous alloy [33]. This assumption allowed to settle the possible temperatures and times of oxidation for a Fe22Cr porous alloy in a 9:1 H_2O:H_2 environment. Nevertheless, in their work, a limited reservoir of Cr inside the alloy particles was not taken into consideration. In this study, the

lifespan is defined as the time for the occurrence of breakaway oxidation, which is a Fe-rich oxide scale formed in the case of depletion of the scale-forming element in the alloy. The same definition of alloy lifespan was applied by Stefan et al., who determined the formation of the breakaway corrosion region for Fe22Cr alloy oxidized at 800°C for ~200 h in air environment [34]. Oxidation tests performed in 2.5% H_2O and 5% H_2/Ar revealed the priority of $(Fe,Cr)_3O_4$ spinel formation, and no breakaway corrosion region was detected.

Koszelow et al. studied the corrosion process of a porous Fe22Cr alloy in the context of its lifespan. They investigated the kinetics of the corrosion process based on the isothermal weight gain obtained at temperatures ranging from 700 °C to 900 °C. Moreover, the chromium content in the alloy was determined after selected time intervals of oxidation [30]. It allowed for the creation of a simple lifespan prediction model for porous alloys based on the data of only 100 hours of oxidation. According to this model, the lifespan of the alloy depends on the chromium reservoir in the alloy. In the earlier work by Huczkowski et al., the authors determined the threshold amount of Cr in the Crofer 22 APU alloy to be 16 wt% [35,36].

Following the parabolic law of oxidation by the Fe22Cr alloy was confirmed in our previous study [26,29]. For chromia forming ferritic alloys, outward Cr-cation diffusion is often cited as the prevalent oxidation mechanism, though with the incorporation of reactive elements, the oxidation mechanism can be modified to be driven by anion inward diffusion [37,38].

The idea of pre-oxidation for chromia-forming alloys means an oxidation at a temperature higher than the intended operation temperature to create a well-defined oxide scale, increase the size of Cr_2O_3 grains and decrease the grain boundaries of the oxide scale. Assuming that the migration of Cr cations is faster in the grain boundaries than within the chromia grains, the effective diffusion flux of Cr cations decreases, a slowdown of the corrosion rate during oxidation at lower temperatures can thus be observed.

Talic et al. investigated the effect of pre-oxidation on the oxidation resistance of dense 0.8 mm – 0.9 mm Crofer 22 APU sheets [39]. They performed pre-oxidation at 900°C for 2 h and at 1100°C for 5 h, followed by oxidation exposures at 800°C. It was confirmed that the oxidation of Crofer 22 APU follows the parabolic rate law. The authors emphasized that the positive impact of pre-oxidation is likely associated with alterations in the Cr species transport characteristics within the thermally formed Cr_2O_3 layer, resulting from a modification of the grain size and/or the defect structure.

Hong et al. investigated the pre-oxidation effect of ferritic T92 stainless steel [40]. They confirmed that the weight gain is 3 times lower for pre-oxidized samples when compared with samples without the pre-oxidation step. There are only a few publications regarding the pre-oxidation process effect on porous ferritic alloys.

Tucker et al. performed pre-oxidation tests of porous P434L (16.66 wt% of Cr, 0.94 wt% of Mo, 0.85 wt% of Si, Fe-balanced) alloy [41]. They revealed ~5 times lower relative weight gain for pre-oxidized (at 850°C for 10 h) samples when compared with the weight gain of as-sintered samples at 700°C in air as well as in a hydrogen/steam environment. The same effect was observed for a LSCF-coated porous P434L alloy in an air and oxygen environment.

Even though the positive effect of the pre-oxidation process was confirmed for dense and porous ferritic alloys, there is still a lack of knowledge about the limitations of this process, including the effect of temperature on pre-oxidation, which can be used to improve the corrosion properties, and the pre-oxidation time. Information about the possible lifespan extension of porous pre-oxidized alloys is missing.

In this study, the pre-oxidation process for porous Fe22Cr alloy was investigated in the context of its possible application at high temperatures, e.g., as SOC support on the air side. The pre-oxidation temperatures were selected based on our previous studies, which revealed experimentally that the lifespan of the porous alloy is >2 000 h at 700°C [30,42]. However, at 900°C the determined lifespan was only ~10 h.

Therefore, for operating at 700°C, the pre-oxidation process was investigated at 850°C and 900°C to provide sufficient oxide scale grain growth and prevent quick breakaway corrosion formation. The X-ray tomography experiments and weight gain measurements allowed us to settle the parameters (temperature and time) of the pre-oxidation process for porous Fe22Cr, which were tested at 700°C and 750°C. These conditions were established based on a correlation between the oxide scale growth expressed by weight gain and 3D microstructure changes observed at different steps of high-temperature oxidation at 850°C. Based on oxidation tests, the selected pre-oxidation conditions were validated.

2. Experimental

2.1. Sample preparation

The sheets of porous Fe22Cr alloy were provided by Höganäs AB. The alloy was produced by a tape-casting method from powder (<53 μm), and the as-received sheet was debinded and sintered in hydrogen (1250°C for 30 min). The composition of the alloy given by the producer is presented in Table 1. This information was confirmed by Inductively Coupled Plasma (ICP) spectroscopy and energy-dispersive X-ray (EDX) measurements. The producer reported the porosity of the alloy as 30%, which was confirmed by the Archimedes method (using kerosene as a medium) as well as by the analysis of scanning electron microscope (SEM) images using dedicated PoroMetric Software (Thermo Fisher). The porosity was evaluated based on the SEM images, as a mean value of results obtained from 20 images taken at 2500x magnification. The measurement uncertainty was calculated as a standard deviation of the mean value obtained from image analysis.

For the oxidation tests, the samples with a size of 10 ×10 mm² were cut from a 0.4-mm-thick porous alloy sheet of Fe22Cr. For the X-ray tomographic study, elongated samples with dimensions of 6 ×1 mm² were prepared. Then the samples were cleaned in acetone, followed by ethanol, for 10 min in an ultrasonic bath.

2.2. Oxidation tests

For the pre-oxidation tests, four series of samples were prepared. Two of them were pre-oxidized at 850°C for 4 h and the remaining two series were pre-oxidized at 900°C for 40 min. One set of samples consisting of a series of samples pre-oxidized at 850°C for 4 h and 900 °C for 40 min, and reference samples (without the pre-oxidation step) were oxidized at 700°C. The second set (the same as the first one) was exposed to 750°C. All oxidation tests were performed in a chamber furnace (Kittec Squadro) in a lab ambient air atmosphere (relative humidity ~30%). For each pre-oxidation process and for the reference samples, 7 samples were used. Detailed information about the oxidation conditions of the investigated samples is presented in Table 2.

The time and temperature of the pre-oxidation were chosen based on our previous study of porous alloys` oxidation in order to obtain ~1% of weight gain after pre-oxidation. The reference samples were investigated to confirm the lifespan extension effect of the pre-oxidized porous alloy. The heating and cooling rates were 180 °C h^{-1} and the full time of oxidation was calculated without these processes. The oxidized samples were removed from the furnace after 250 h intervals in order to weigh them using a microbalance Radwag XA 5Y.M. with an accuracy of 1 μg.

The weight gain of the samples was calculated as a relative (percentage) mass change with respect to the initial sample mass. In the weight gain plots, the points represent the average mass change for the set of samples. The weight changes were also recalculated taking into consideration the specific surface area information, which is 0.022 cm² g^{-1} (obtained from the tomographic study presented in our previous work [29]). The oxidation tests were terminated for selected samples in order to perform post-mortem analysis.

Table 1

A composition of the porous Fe22Cr alloy given by the producer.

Element	Fe	Cr	Mn	Mo	Cu	Si	Ni	C	Nb
wt%	Bal.	22	0.23	0.01	0.02	0.08	0.03	0.01	0.02

Table 2

Oxidation conditions of the investigated porous Fe22Cr alloys.

Set no.	Preoxidation temperature [°C]	Preoxidation time [min]	Oxidation temperature [°C]
1	900	40	700
2	850	240	700
3	900	40	750
4	850	240	750

2.3. Chromium evaporation

Cr(VI) evaporation measurements were carried out in horizontal tube furnaces using an airflow of 6000 sl•min-1 for up to 500 h. Cr(VI) vaporization is a significant issue in terms of the longevity of the fuel cell stack. Therefore, it is necessary to quantify the rate of Cr(VI) evaporation during the exposure. Cr(VI) vaporization was measured for all samples using the denuder technique, which allows in situ determinations of Cr(VI) evaporation. A detailed description of the Cr(VI) evaporation measurement procedure can be found elsewhere [43]. At least two sets of three samples were exposed, and Cr(VI) evaporation measurements were performed at regular intervals.

2.4. Synchrotron tomographic microscopy

In order to validate the positive effect of the chosen pre-oxidation conditions ($\sim$1 wt% weight gain), the X-ray tomographic study was performed at the TOMCAT beamline of the Swiss Light Source (SLS) at the Paul Scherrer Institute, Villigen, Switzerland. The cut and cleaned rectangle-shaped sample was stuck to the metallic holder using wax to prevent any horizontal or vertical motion during the experiment. A parallel X-ray beam with an energy of 40 keV was used. The detector configuration comprised a scintillator that turned X-rays into visible light, an objective lens, and a sCMOS camera that generated an image characterized by a pixel size of 0.325 μm and a field of view of around 0.8 mm$\times$0.7 mm. With a total of 1001 projections across 180° recorded, each with a 1600 ms exposure, scans took roughly 26 minutes to complete. The scans were performed for the sample after selected time intervals of oxidation in air at 850 °C using a heat blower. A thermocouple indicated that the temperature fluctuation was $\sim$5 °C. The tomograms were generated for the sample after 3 h, 5.5 h, 7.5 h, 10 h, 12.5 h, 15 h, 17.5 h, 20 h, 22.5 h, 25 h, 27.5 h, and 30 h of oxidation.

The collected tomograms were reconstructed utilizing the in-house developed pipeline accessible at the beamline, which gives entire tomographic volumes immediately after the data acquisition and enables the rapid modification of the measurement and reconstruction algorithm parameters. The obtained projections were tomographically reconstructed after dark- and flat-field correction and phase retrieval (according to the Paganin method [44]). Signal-to-noise and contrast-to-noise ratios were improved with the use of phase retrieval. The achieved contrast in the images reconstructed with this approach allowed for a relatively straightforward material segmentation based only on intensity thresholding, which was performed using the commercial software Thermo Scientific Avizo 9.4. The intensity ranges assigned to the steel, porosity, and oxide scales were determined based on the histogram minima for one of the samples with a significant degree of oxidation. For phase segmentation, the same intensity ranges were then applied to the measured tomograms. Although the absolute values of estimated material percentages are dependent on the intensity thresholds chosen, applying the same intensity ranges to all samples

enables a realistic comparison of oxidation-induced changes. It was noted that for these tomographic measurements, it is possible to distinguish objects of $\sim$1.5 μm in the reconstructed volumes; hence, 1.5 μm was regarded as the resolution of the analyzed images.

2.5. Scanning electron microscopy analysis

In order to evaluate the morphology changes of pre-oxidized samples after further oxidation at lower temperatures, scanning electron microscopy was employed. The images of porous alloys oxidized without a pre-oxidation step were taken as references. SEM imaging was performed using a Phenom XL electron microscope (Thermo Fisher Scientific, Netherlands) on polished cross-sections of the samples. All SEM images were recorded using a backscatter electron detector (BSE). The microscope was equipped with an EDX detector (Thermo Fisher Scientific, 25 mm^2 Silicon Drift Detector), which was used for elemental analysis of steel (EDX analyses performed at an acceleration voltage of 15 kV).

The morphology changes of porous alloys that are caused by the oxidation process are crucial for determining the effect of pre-oxidation. Thus, in this work, morphology changes as well as phase composition are evaluated in detail for the first hours of oxidation.

2.6. Transmission electron microscopy analysis

The samples for TEM imaging were prepared as lamellae. They were prepared by sputtering the sample surface with Ga$^+$ ions emitted from a liquid metal ion source (FIB). The lamellae were finished with thinning down to a level of several dozen nanometers after being mounted in a TEM-dedicated copper grid.

The TEM/STEM analyses were performed using a Cs probe-corrected Titan Cubed G2 60–300 microscope (FEI) equipped with the ChemiSTEM™ system. High-resolution STEM (HRSTEM) images were acquired using a high-angle annular dark-field (HAADF) detector.

3. Results and discussion

3.1. Non-oxidized alloy analysis

The surface morphology and cross-sectional microstructure of the unoxidized porous Fe22Cr alloy are presented in Fig. 1. The necks between particles are clearly visible for both surface (Fig. 1 D) and cross-sectional (Fig. 1 B) images. The porosity of the alloy is easily recognizable, even for low magnification images (Fig. 1 A, C). Using the Archimedes method, the porosity was calculated as (30 $\pm$ 2) %. The SEM image analysis method revealed (29 $\pm$ 5) % porosity, which is in agreement with both the Archimedes method and the value given by the producer ($\sim$30%) data.

The composition of the investigated alloy, determined by the producer, is shown in Table 1. For confirmation of this data, Inductively Coupled Plasma Spectroscopy (ICP) and EDX measurements were performed. The obtained compositions are presented in Table 3. The ICP data corresponds with the composition provided by the producer. The EDX measurement revealed some small differences in the Cr and Mn levels. However, taking into consideration limitations in the accuracy of this technique, the resultant composition of the investigated alloy corresponds well with the producer data.
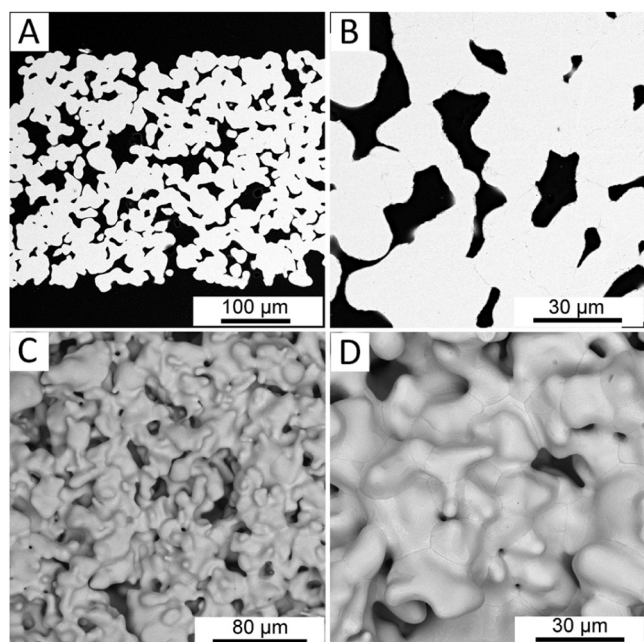
Fig. 1. SEM images of A, B) cross-section; C, D) surface of as-received Fe22Cr alloy.

3.2. Pre-oxidized samples morphology

The impact of the pre-oxidation process on the longevity of porous alloys is determined by modifications in the fluxes of grain and grain boundary diffusion. For the evaluation of this effect, a detailed morphology analysis is necessary. In Fig. 2, SEM images of a porous alloy surface are presented. In the first row (Fig. 2 A – C), images of the Fe22Cr alloy pre-oxidized at 850°C are shown. The second-row images illustrate the porous Fe22Cr alloy pre-oxidized at 900°C for 40 min.

The images of the samples after the pre-oxidation taken at 2000 x magnification (Fig. 2 A and D) reveal well-connected particles with easily observed necks between them. The oxide scale phase is noticeable on the particle surface for both considered samples. At this low magnification, no significant morphological difference between the porous alloy pre-oxidized at 850°C for 4 h and pre-oxidized at 900°C for 40 min is visible.

For the alloys` images taken at 5000 x magnification (Fig. 2 B and E for the Fe22Cr alloy pre-oxidized at 850°C for 4 h and pre-oxidized at 900°C for 40 min, respectively), the oxide scale is easily detectable on the particle surface. A difference in chromia crystal size is observed between the considered samples. Based on the images taken at 5000 x magnification, it seems that bigger chromia crystals could be detected for the sample pre-oxidized at 850°C for 4 h than for the sample pre-oxidized at 900°C for 40 min.

Images taken at 10 000 x magnification for the alloy pre-oxidized at 850°C for 4 h and pre-oxidized at 900°C for 40 min are shown in Fig. 2 C and F, respectively. Microstructural differences are easily observed when comparing the oxide scale crystals size. Chromia crystals are larger for the sample pre-oxidized at 850°C for 4 h – their width reaches up to 5 μm. On the other hand, chromia crystals observed on the surface of the porous alloy pre-oxidized at 900°C for 40 min are ∼ 1 – 2 μm in width.

In Fig. 3 SEM images of the cross-section of the porous Fe22Cr alloy pre-oxidized at 900°C for 40 min are presented. The images were obtained by Focus Ion Beam preparation of the sample for TEM imaging. The analysis of the pre-oxidized sample image (Fig. 3A) reveals the slightly visible oxide scale on the alloy surface. Nevertheless, the thickness of the oxide scale is <0.5 μm, therefore the morphology of the

Table 3
Chemical composition of the alloys obtained from ICP and EDX measurements.

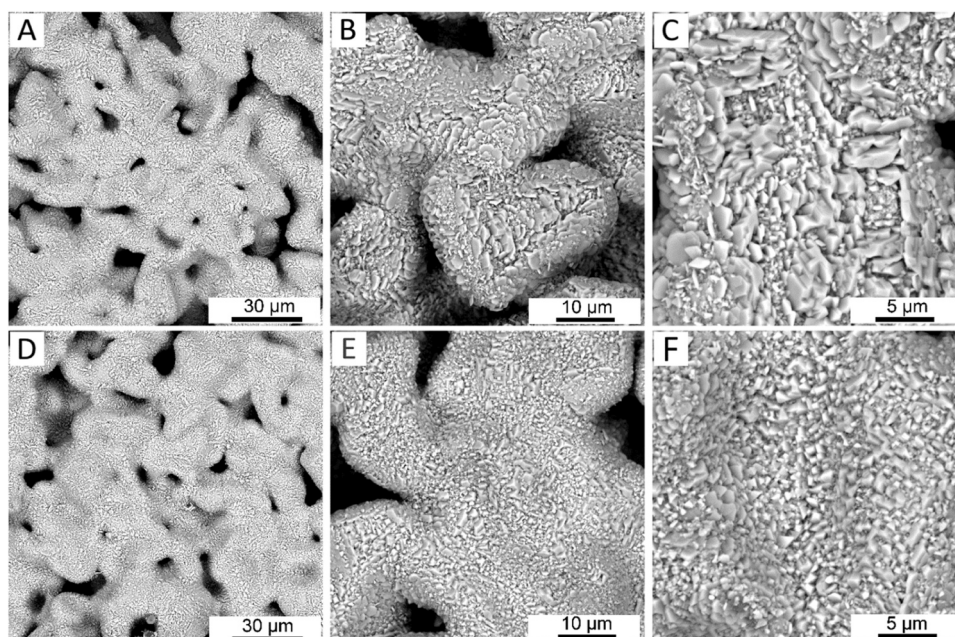| Target composition | Fe | Analysed chemical composition, wt% [information from the ICP measurement] | | | | | | | | EDX, wt% | |
		Cr	Mn	Ni	Si	Ti	Co	Ca	Na	Cr	Mn
Fe22Cr	Bal.	21.87	0.25	0.02	0.08	0.01	0.01	0.00	0.00	21.3	0.1

Fig. 2. SEM images of the alloy surface after (a-c) pre oxidation at 850°C for 4 h, (d-f) pre-oxidation at 900°C for 40 min.
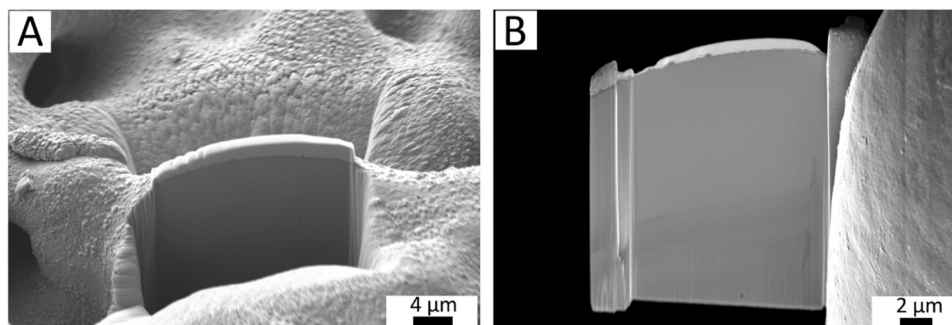
Fig. 3. SEM images of the porous Fe22Cr cross-section after pre-oxidiation at 900 °C for 40 min taken at A) 2000 x, and B) 4000 x magnification.

pre-oxidized samples is macroscopically similar to the raw samples presented in Fig. 1A - B. For the images taken at 4000 x magnification (Fig. 3B) the continuous oxide scale layer can be recognized on the surface of alloy particles. The thickness of the oxide scale is below 0.5 μm.

3.3. Pre-oxidation conditions validation via 3D microstructure analysis

In spite of the fact that SEM imaging is a technique that allows for the evaluation of the oxide scale thickness for different samples, it can also be misleading. A specific polished cross-section might not be representative for determining the microstructure of the sample, especially for porous samples, which consist of many different-size particles that form a high-specific surface area structure. In order to observe the microstructural changes of porous metallic alloys, a 3D analysis is necessary. Thus, synchrotron tomography was employed to analyze the selected samples.

The visualization of the sample oxidized at 850 °C for 5.5 h obtained by volume rendering of the reconstructed slices is presented in Fig. 4A. The necks between the alloy particles are easily observed, as well as the porosity of the sample. Phase contrast allows for distinguishing the metallic core, oxide scale, and porosity phases. Thus, material segmentation was performed based on the different gray scales of each phase. An exemplary slice of the selected piece of the reconstructed volume that was used for detailed analysis is presented in Fig. 4B. The segmentation of the selected volume is illustrated in Fig. 4C, where orange is assigned to the oxide scale, and the metallic core is represented by turquoise.

The investigated time intervals of the tomographic analyses (3 h and 5.5 h) are not exactly the same as the pre-oxidation process performed at 850 °C (4 h). It means that the observed microstructural changes cannot be directly compared with the microscopic data obtained with SEM analysis. Nevertheless, tomographic measurements enable the observation of microstructural changes both before and after the chosen pre-

oxidation time. Therefore, the analysis of the tomographic data conclusively allows for the validation of the required pre-oxidation time to achieve a positive impact on the alloy lifespan.

In Fig. 5, the results of material segmentation for the Fe22Cr alloy before (Fig. 5 A) and after different times of pre-oxidation (3 h, 5.5 h, and 30 h for Fig. 5B-D, respectively) performed at 850 °C are presented. The different colors are assigned to the particular phase: the oxide scale is represented by orange, and the metallic core is represented by turquoise. For each of these images, the same region of sample was selected in order to observe the microstructural changes during the oxidation process. For the unoxidized sample (Fig. 5A) the necks between particles are clearly visible, as are the pores within the whole sample`s volume. The surface of the metallic core is smooth, and no signs of oxide scale were detected.

After 3 h of oxidation (Fig. 5B) the oxide scale is apparent, but there are still regions without visible chromia on the alloy`s surface (marked by the black arrow). However, the resolution of the tomographic measurements is ~1.5 μm. Therefore, it seems likely that the oxide scale thickness does not exceed 1.5 μm and it cannot be recognized via microtomographic techniques. For the sample oxidized for 5.5 h at 850 °C (Fig. 5C), the regions of the uncovered alloy`s surface are still observed (marked by the black arrows). However, the first signs of oxide scale can be recognized in the place that corresponds with the region marked by the black arrow in Fig. 5B. In Table 4 a relative volume for each detected phase is summarized. A small difference in the oxide scale amount between the sample oxidized for 3 h and 5.5 h (from 23.9 vol% to 24.6 vol%) indicates that even longer pre-oxidation time than assumed 4 h, that cause ~1 wt% weight gain, can be applied to achieve a positive effect from the pre-oxidation process.

After 30 h of oxidation at 850 °C, the oxide scale was detected not only on the whole alloy surface but also inside the alloy`s particles (Fig. 5 D). Moreover, in some regions, the extension of the oxide scale regions occurred. This observation is consistent with the tomographic
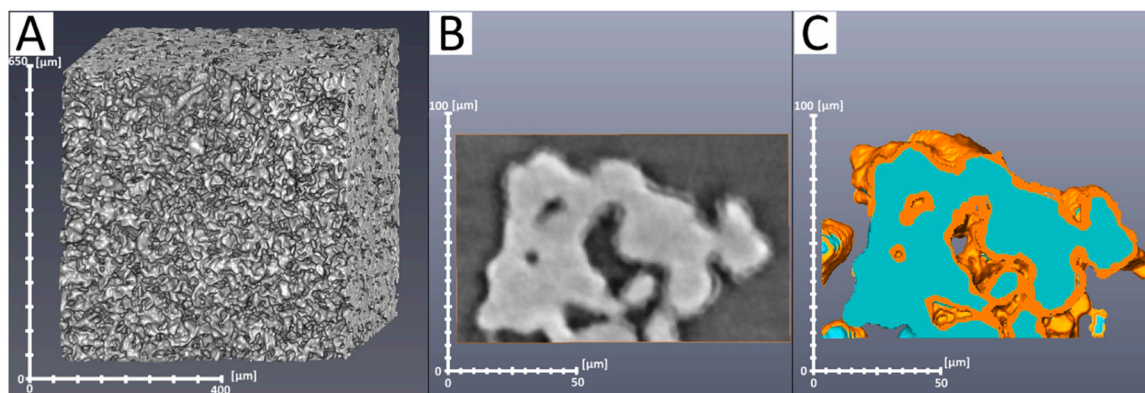

Fig. 4. A) Visualisation of the sample oxidized at 850 °C for 5.5 h obtained by volume rendering of the reconstructed slices, B) exemplary slice of the sample region selected to the detailed analysis, C) material segmentation of the chosen reconstructed volume.
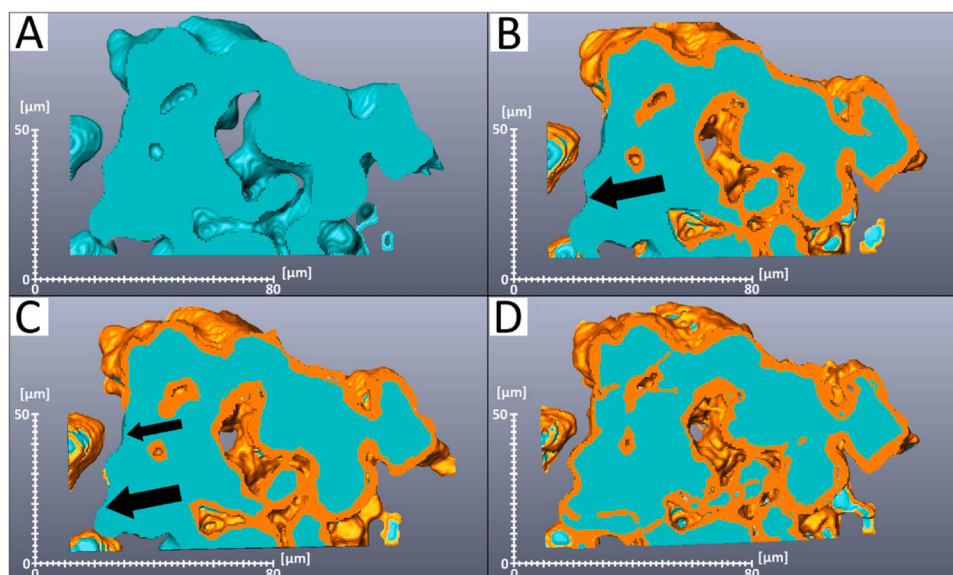
Fig. 5. Material segmentation for the Fe22Cr alloy (a) before and (b-d) after 3 h, 5.5 h and 30 h of oxidation performed at 850°C, respectively.

Table 4
Material statistics after oxidation at 850°C.

Time of oxidation [h]	Alloy [vol%]	Oxide scale [vol%]
3	76.1	23.9
5.5	75.4	24.6
30	68.9	31.1

analysis of the Fe22Cr alloy performed in our previous study [42]. The relative oxide scale volume increased from 24.6% after 5.5 h of oxidation to 31.1% after 30 h at the same temperature. The oxidation at 850°C (and higher) leads to fast formation of breakaway corrosion when 6 wt% of relative weight gain is reached (based on our previous study). On the other hand, oxidation at high temperatures can be applied for a shorter time for the pre-oxidation process.

3.4. Oxide scale growth kinetics at 700°C

The relative weight gain for all investigated porous Fe22Cr samples is presented in Fig. 6. The first set of samples was pre-oxidized at 900 °C for 40 min, and the second one was pre-oxidized at 850 °C for 4 h. The weight gain after the pre-oxidation steps was 1.05% and 1.12%, respectively. Then, further exposure of the samples was performed at 700 °C (Fig. 6A and C). The relative weight gain for the pre-oxidized

samples is significantly lower when compared with the reference samples (oxidized at 700°C without the pre-oxidation step). For the reference samples, a threshold value of 6 wt% in relative weight gain was reached after 1500 h of oxidation at 700°C.

The samples pre-oxidized at 900°C for 40 min reveal lower relative weight gain than samples pre-oxidized at 850°C for 4 h. Our previous study of porous alloys` long-term performance disclosed that ~ 6 wt% is a threshold value of relative weight gain for breakaway corrosion appearance in Fe22Cr alloys. The same relative weight gain data as in Fig. 6A is also presented in a log-log scale, as shown in Fig. 6C. The cross point between the linear extrapolation of the relative weight gain data and the dashed line, which represents the threshold value of 6 wt% indicates the predicted lifespan of the alloy. The lifespan of the alloy pre-oxidized at 900°C for 40 min was calculated as (3765 ± 450) h, and for the alloy pre-oxidized at 850°C for 4 h, the lifespan was (2220 ± 310) h. The measurement uncertainty for the lifespan estimation was calculated taking into consideration the 95% prediction band. The uncertainty of the weight gain measurements was counted as the standard deviation of the mean. Then, the weight gain of the samples pre-oxidized at 850°C for 4 h and further 2000 h oxidation at 700°C was (5.41 ± 0.73) %. This weight gain range reached the threshold limit of 6 wt%, thus the obtained result indicates breakaway corrosion region appearance in this case. For the samples pre-oxidized at 900 °C, the measured weight gain after 2000 h of oxidation at 700°C was much lower: 3.91 wt%.

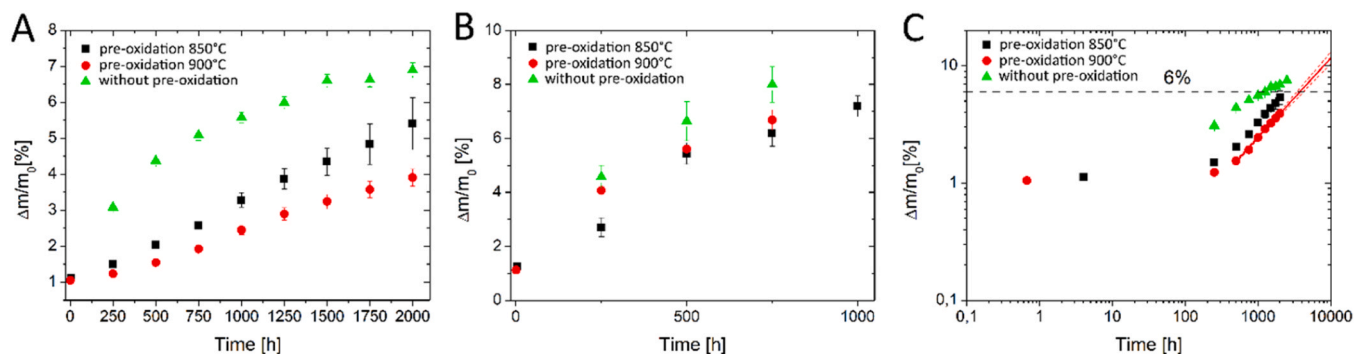The weight gain measurements allow for the determination of the

Fig. 6. Percentage mass change of raw, pre-oxidized at 850°C for 4 h and pre-oxidized at 900°C for 40 min alloys oxidized at (a) 700°C for 2000 h and (b) 750°C for 1000 h. (c) Log-log plot the data presented in (a) with the lifespan prediction lines. The 6 wt% dash line represents the assumed threshold level for the breakaway corrosion appearance.

oxidation kinetics for the investigated alloy. Based on the weight gain data illustrated in the log-log scale (Fig. 6 C), the slope of the curves was calculated using linear regression. For the pre-oxidized samples, two of the first points were excluded from the analysis. For the reference samples, the calculated slope was 0.42, and for both series of pre-oxidized samples it was 0.69. This change of slope indicates that another mechanism started to determine the oxidation kinetics of the investigated alloy after the pre-oxidation step. This is analyzed in detail in Section 3.9.

The available literature data as well as our previous study reveal that Cr-based ferritic alloys follow a parabolic law of corrosion expressed by equation $\left(\frac{\Delta m}{S}\right)^2 = k_p t$, where Δm [g] is the weight gain of the sample, S is the surface area of the alloy [cm^2], t is time of oxidation [s], and k_p is the parabolic rate constant [g^2 cm^{-4} s^{-1}]. Based on the available surface area data for the Fe22Cr alloy determined in our previous work (220 cm^2 g^{-1}), weight gain data has been recalculated per surface area, which allowed to calculate corrosion rate parameters for comparison with data from bulk alloys (Figure S.3.). The parabolic rate constant of the corrosion process found in this study is 1.2×10^{-14} g^2 cm^{-4} s^{-1} for raw samples, 9.7×10^{-15} g^2 cm^{-4} s^{-1} for samples pre-oxidized at 850°C, and 5.1×10^{-15} g^2 cm^{-4} s^{-1} for samples pre-oxidized at 900°C. In our previous study, the k_p value was determined for the same porous Fe22Cr alloy as 4.5×10^{-15} g^2 cm^{-4} s^{-1} for oxidation at 700 °C (without the pre-oxidation step). The difference between these results is due to the character of the oxidation experiments: in our former work we carried out short term isothermal exposures, whereas in the present work, we carry out long term cyclic exposures. The value obtained for raw alloys agrees with the literature data for similar alloys (Crofer 22 APU/H). Falk-Windisch et al. calculated the k_p value for Crofer 22 H as 4.5×10^{-16}, 1.1×10^{-14} and 3.3×10^{-13} g^2 cm^{-4} s^{-1} for 650, 750, and 850 °C, respectively [45]. Stefan et al. obtained the k_p values of 8×10^{-15} g^2 cm^{-4} s^{-1} and 1×10^{-12} g^2 cm^{-4} s^{-1} from the oxidation tests performed for porous Fe20Cr alloy at 700 °C and 800 °C, respectively [46].

3.5. Oxide scale growth kinetics at 750°C

Fig. 6 B shows the relative weight gain of samples that were pre-oxidized at 900°C for 40 minutes and 850°C for 4 hours, during oxidation at 750°C (sets no. 3 and 4 in Table 2). The weight gains were 1.26% and 1.12%, respectively. Like the samples that were oxidized at 700°C, the reference alloy, that was oxidized at 750°C without the pre-oxidation step, showed the highest relative weight gain when compared to the samples that had already been pre-oxidized. The difference in weight gain between the alloys pre-oxidized at 850°C for 4 h and the alloys pre-oxidized at 900°C for 40 min is negligible after 500 h of oxidation. After 750 h of oxidation at 750 °C, the higher increase in weight gain for samples pre-oxidized at 900°C for 40 min is noticeable. In contrast to the samples pre-oxidized at 850°C for 4 h, for samples pre-oxidized at 900°C for 40 min, breakaway corrosion regions were detected (Figure S.2. in supplementary materials).

3.6. Cr evaporation

In addition to oxidation kinetics, Cr evaporation from porous alloys has been determined. The results of Cr evaporation for raw samples, pre-oxidized alloys at 850°C for 4 h, and pre-oxidized alloys at 900°C for 40 min are presented in Fig. 7 A-C, respectively. The cumulative Cr evaporation curves reveal only slight changes between raw alloy oxidation and the oxidation of pre-oxidized alloys. The highest total Cr evaporation is observed for the alloy pre-oxidized at 900°C for 40 min, which is 2.32×10^{-4} mg cm^{-2} after 500 h and the lowest one is 1.57×10^{-4} mg cm^{-2} for the alloy pre-oxidized at 850°C for 4 h. The Cr evaporation rate is also comparable for all investigated samples, and varies from $\sim 2 \times 10^{-7}$ mg cm^{-2} h^{-1} to 8×10^{-7} mg cm^{-2} h^{-1}. No significant difference between the Cr evaporation of raw alloys and pre-oxidized alloys is visible. It seems that the pre-oxidation process does not significantly change the rate of Cr evaporation from the alloy.

The chromia present on the alloy surface undergoes evaporation, due to the formation of volatile hexavalent Cr species. These compounds constitute the reason for the deterioration of the oxygen electrode in SOC systems [14,45]. Therefore, the influence of Cr evaporation for the ferritic Cr-based ferritic alloys was investigated, especially in the context of potential interconnector material in SOCs [47–50].

Falk-Windisch et al. studied the effect of temperature on chromium vaporization and oxide scale growth for Crofer 22 H and Sanergy HT alloys [45]. They performed Cr evaporation measurements at 650°C, 750°C, and 850°C for 500 h, revealing that both steels showed rather similar oxidation and vaporization behavior. Furthermore, they demonstrated that a decrease in temperature of 100°C results in a fivefold reduction in overall weight gain, but the vaporization of Cr decreases by a factor of 2–3.

Reisert et al. investigated Cr evaporation for a 434 L porous alloy pre-oxidized at 850°C for 10 h in air with 3% of H$_2$O [51]. The specific surface area of the studied alloy was 0.025 m^2 g^{-1}. The obtained Cr evaporation rate was 6.3×10^{-6} mg cm^{-2} h^{-1}. The higher value compared with this work is due to the lower temperature and humidity in the present experiments.

However, the Cr evaporation rate curves for the porous Fe22Cr alloy (Fig. 7) do not reveal the same tendency as it was indicated by other studies for bulk alloys with similar chemical composition [47,52,53]. It may be connected with a higher specific surface area for the porous alloy, so the larger possible area for the evaporation process. Moreover, the level of Mn within the alloy particles is possibly insufficient to form a Mn-rich spinel layer on their surface, thus the linear trend of the evaporated Cr is observed for the investigated alloy.

Koszelow et al. proved that based on the changes in Cr content inside the alloy particles, it is possible to estimate the possible lifespan of the porous Cr-based alloy [29]. Since there isn't a clear difference between reference and pre-oxidized alloys in terms of Cr evaporation, it may indicate that the pre-oxidation process doesn't have a significant effect on the oxide scale growth and thus, it does not influence the alloy's lifespan. The Cr evaporation rate for the raw alloy is noticeably higher than for the pre-oxidized samples for the first hundred hours of the
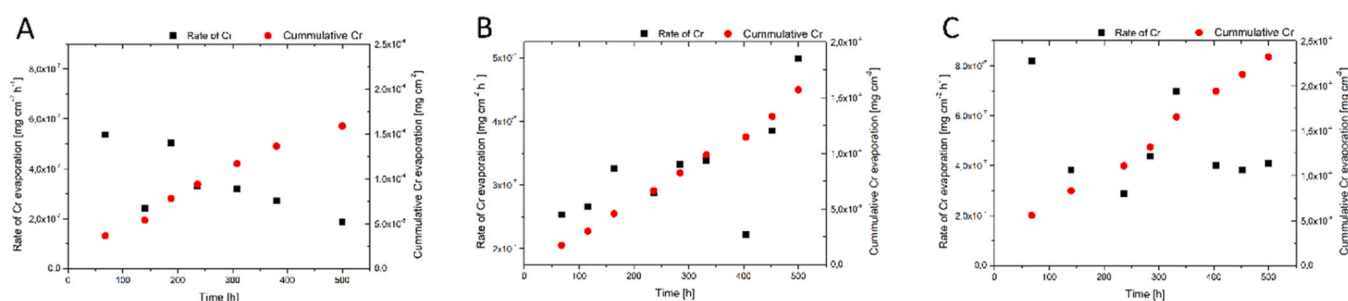

Fig. 7. The results of Cr evaporation for (a) raw samples (b) alloy pre-oxidized at 850°C for 4 h, (c) alloy pre-oxidized at 900°C for 40 min.

exposure. It corresponds with the weight gain results that revealed a significantly higher weight increase for raw samples when compared with the pre-oxidized samples (see Fig. 6 A). This shift in weight gain is also visible in the log-log plot (see Fig. 6 C).

3.7. Morphological SEM analysis after aging

According to the oxidation model, breakaway corrosion regions should be apparent for the sample pre-oxidized at 850°C for 4 h and further oxidized at 700°C for 2000 h. To validate the lifespan prediction model, SEM was employed for the pre-oxidized and aged samples. In Fig. 8, SEM images of the pre-oxidized and aged samples for 2000 h at 700°C are shown.

In the first row (Fig. 8A - C) the porous pre-oxidized at 850°C for 4 h and further oxidized at 700°C for 2000 h Fe22Cr alloy was shown. The image taken at 700 x magnification (Fig. 8A) reveals the breakaway corrosion region. It is in agreement with the oxidation exposure measurements (Fig. 6A), which show that the threshold weight gain limit (6 wt%) was reached for the porous alloy pre-oxidized at 850°C and further sintered at 700°C for 2000 h. However, a large region without breakaway corrosion is observed for this sample. It means that the alloy is at the beginning of breakaway corrosion formation.

The images taken at 2000 x and 5000 x magnification (Fig. 8B and C, respectively) allow for determining the chromia thickness, which is ∼ 3 µm. The oxide scale is apparent on the whole alloy surface, and it tightly covers all particles. Moreover, the oxide scale seems to occupy the pore regions observed before oxidation. The phenomenon of replacing the pore volume by the formation of the oxide scale was confirmed in our previous work [42].

The second-row images (Fig. 8D - F) show the porous Fe22Cr alloy pre-oxidized at 900°C for 40 min and further oxidized at 700°C for 2000 h. At lower magnification (Fig. 8D), the oxide scale is easily detectable on the particle surface. However, no signs of breakaway corrosion regions are observed. It corresponds to the weight gain measurements (3.91% of weight gain after 2000 h of oxidation at 700°C) and

the lifespan prediction model, which indicate that breakaway corrosion might be apparent only after 3800 h ± 400 h.

Higher magnification images of the porous Fe22Cr alloy pre-oxidized at 900°C for 40 min and further oxidized at 700°C for 2000 h are presented in Fig. 8 E and Fig. 8 F (taken at 2000 x and 5000 x, respectively). The chromia layer seems to be smooth and tightly covers the whole alloy surface. The thickness of the oxide scale is ∼ 2 µm.

3.8. Grain size changes (TEM analysis)

Detailed characterization of the alloy-oxide was carried out on the FIB-cut lamellae by STEM. The analysis of the sample pre-oxidized at 900°C for 40 min was performed to determine the microstructural changes of the oxide scale, especially in the context of chromia grain size (Fig. 9). The analysis of the alloy pre-oxidized at 900°C for 40 min after further oxidation at 700°C for 2000 h was performed to observe the microstructural changes in detail (Fig. 10).

In Fig. 9A, the structure of the oxide scale layer is presented. A continuous layer of chromia is visible on the top of the alloy surface. The thickness of the oxide scale layer is in the range of 100 nm to 350 nm. Nevertheless, the voids between alloy and oxide scale are also detected, which is consistent with our previous study of long-term oxidized Fe22Cr alloy [26]. For the Fe22Cr alloy pre-oxidized at 900°C for 40 min and further oxidized at 700°C for 2000 h the oxide scale thickness is in the range from 3 µm to 4 µm (Fig. 10A). The voids between alloy and chromia are also visible.

In Fig. 9B, a higher magnification image of the alloy-oxide scale interface is presented. The voids are clearly observed, and their width ranges from ~70 nm to ~150 nm. Moreover, the differences in the oxide scale thickness are also visible, as shown in Fig. 9A. On the other hand, the higher magnification image of the pre-oxidized sample after further 2000 h oxidation reveals the elongated shape of the chromia grains, which form near the oxide scale-air interface. The width of these chromia grains is in the range from 0.5 µm to 1.5 µm. However, the oxide scale grains placed near the alloy particles are undistinguishable.
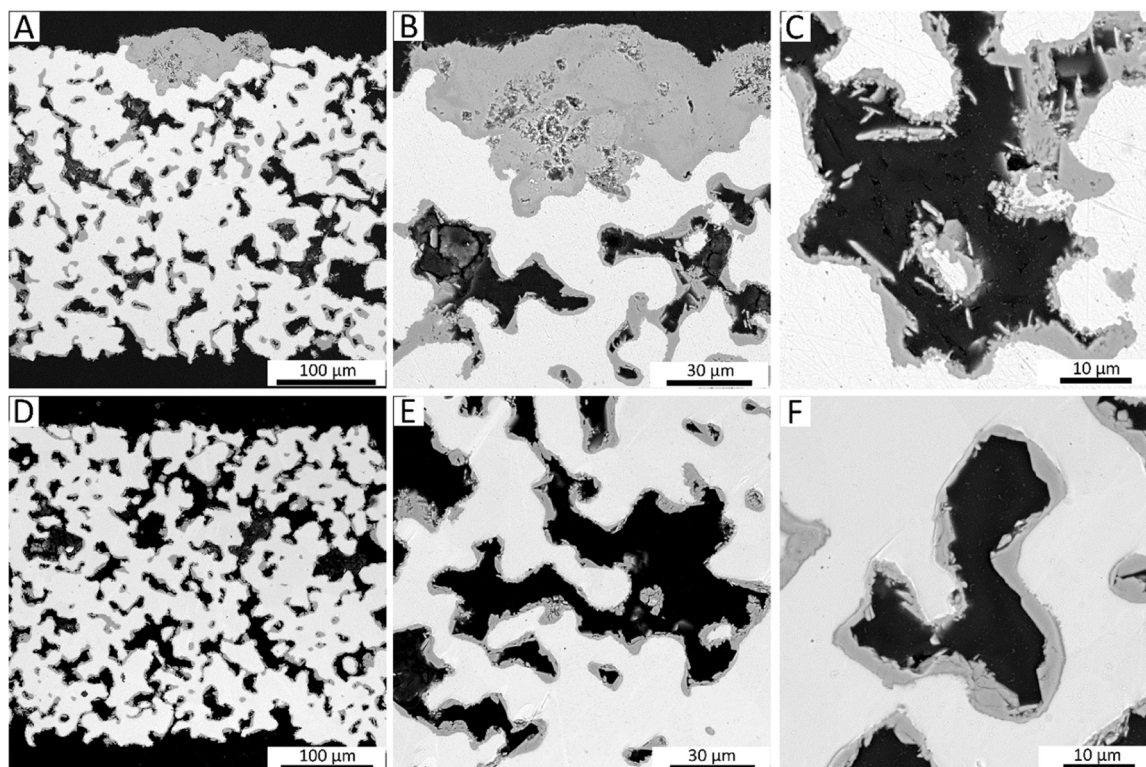

Fig. 8. SEM images of the pre-oxidized at A-C) 850°C for 4 h, and D-F) 900°C for 40 min Fe22Cr alloy after further 2000 h of oxidation at 700°C.
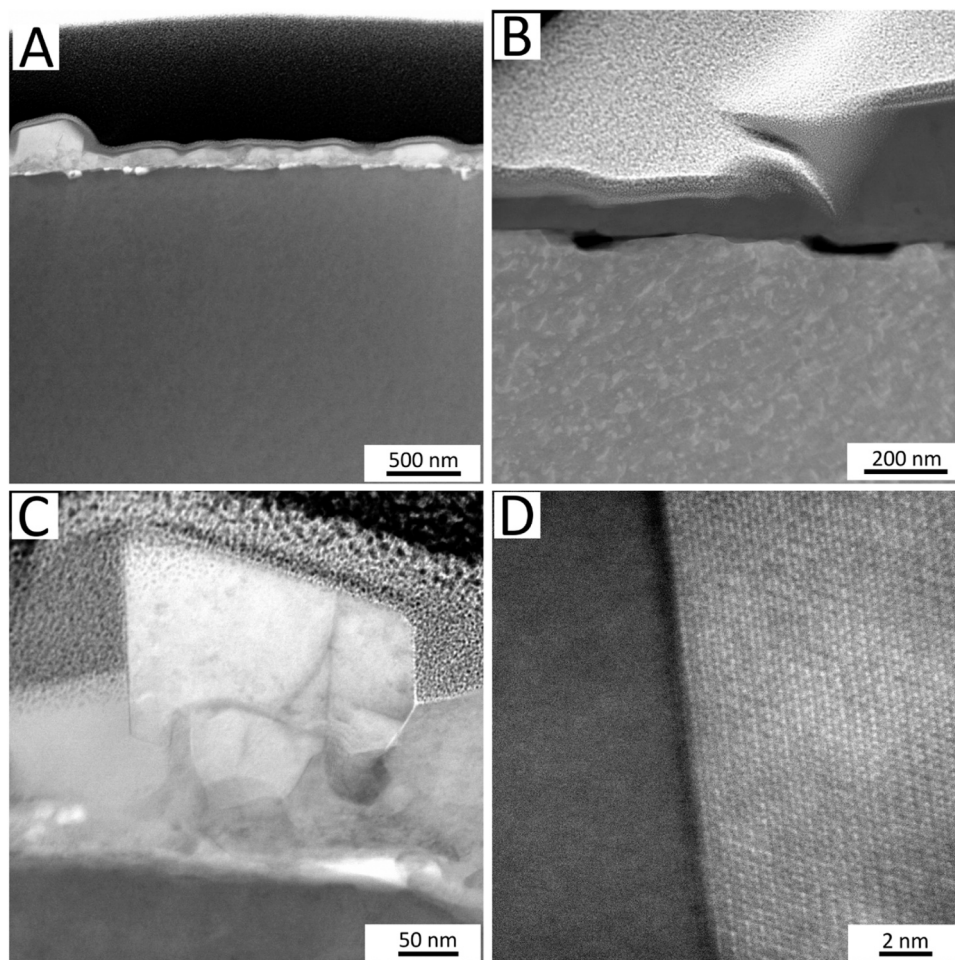
Fig. 9. TEM images of the porous Fe22Cr alloy pre-oxidized at 900°C for 40 min.

A detailed microstructure analysis of the oxide scale grains is presented in Fig. 9C. The grain size in the oxide scale layer differs between the alloy-oxide scale and oxide scale-air interfaces, similar to the sample aged at 700°C for 2000 h. The grains of the chromia at the alloy-oxide scale interface are undistinguishable. On the other hand, the oxide scale grains, which are located near the air, have a size range of ~50 nm to 150 nm. The grain boundary between these huge grains is presented in Fig. 9D. It is revealed that the grain boundary is incoherent, so the neighboring crystals are oriented in different directions. Thus, the diffusion of Cr species is probably determined by the grain boundary diffusion coefficient.

In Fig. 10C-D the alloy-oxide scale interface is presented at higher magnifications. The size of some oxide scale grains can be estimated as to be in the range from 25 nm to 50 nm. Nevertheless, some of the oxide scale grains do not reveal clear grain boundaries, so their size cannot be easily determined. In addition to that, the darker regions within the oxide scale layer might indicate different phases.

The EDX analysis of the oxide scale layer formed after pre-oxidation at 900°C and further oxidation at 700°C for 2000 h is presented in Figure S.5 and Figure S.6 in the supplementary part of this work. The analysis revealed the presence of elements such as Cr, O, and Fe in the examined alloy. Notably, the absence of detectable manganese can be attributed to its low concentration in the alloy (0.2 wt%). The significant presence of iron-rich regions within the oxide scale may indicate the onset of breakaway corrosion formation for the investigated alloy. This conjecture is reinforced by the detected quantity of Cr in the steel, which amounts to ~14 wt%. However, there is also a possibility that the presence of an iron-rich phase near the alloy – oxide scale interface is possible due to Fe diffusion from the alloy to the oxide scale. Sabioni et al. investigated the diffusivities of Fe and Cr within the chromia formed on Fe15Cr alloy [54]. They revealed that the effective diffusion of Fe is greater than the diffusion of Cr at 750°C. On the other hand, the chromia formed on a Fe15Cr alloy was called as 'thermodynamic barrier' for iron diffusion because of the very low oxygen pressure at the alloy – oxide scale interface.

3.9. Discussion of a grain boundary diffusion mechanism

The pre-oxidation process influences the number of grain boundaries of Cr species in chromia via an induced increase of chromia grain size [55–62]. The outward Cr^{3+} cation diffusion is directly connected with the microstructure of the oxide scale for Cr-based ferritic alloys. The presence of structural defects like dislocations or grain boundaries leads to an increase in the effective diffusion coefficient. Moreover, it was proved that there is a direct connection between the parabolic weight gain and the diffusion mechanism because the transport of reactants (cations or anions) through an oxide scale is a diffusion-limited process for ferritic alloys [57].

The slope of the curves obtained from the linear regression of the weight gain data (Fig. 6C) changes from 0.42 (for raw alloys) to 0.69 (for both pre-oxidized sets of samples). From the slope change analysis, the two first points were excluded for the pre-oxidized samples. Despite the higher value of the slope of the weight gain data for the pre-oxidized samples, which could indicate shortening the lifespan of the alloy, the lifespan extension for these samples is observed in comparison to the raw alloy.
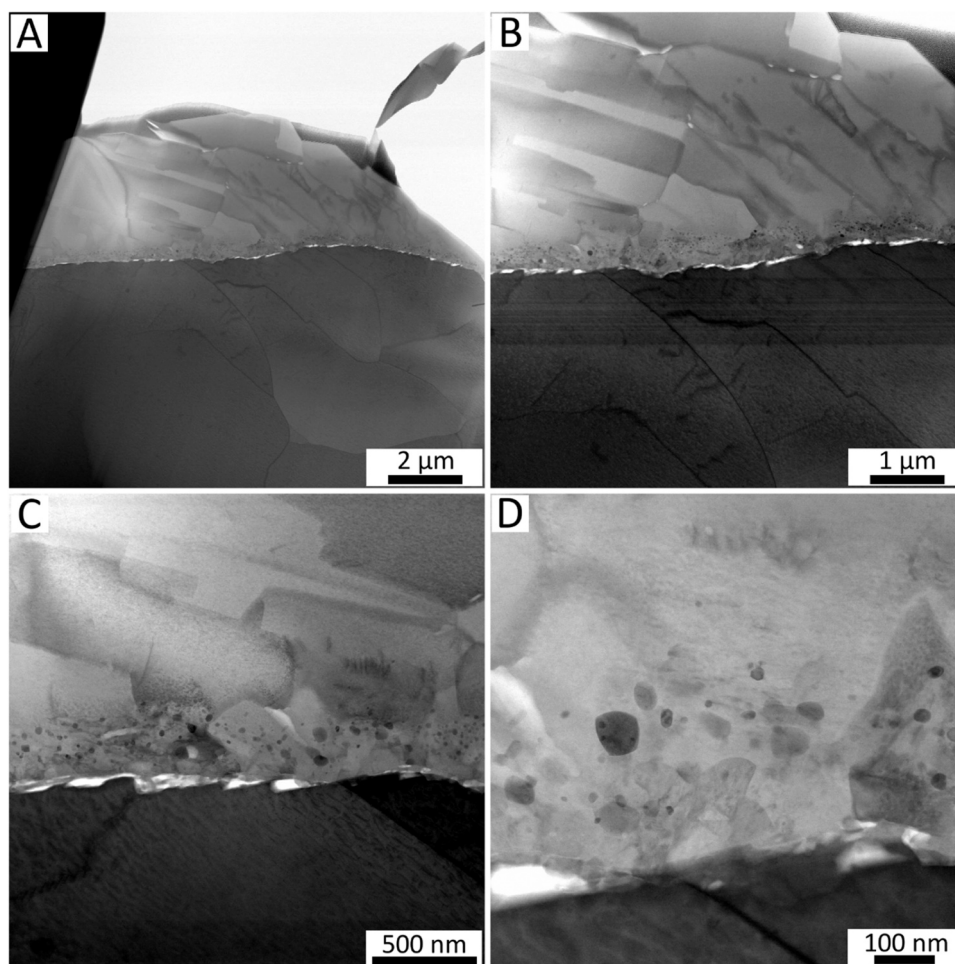
Fig. 10. TEM images of the porous Fe22Cr alloy pre-oxidized at 900°C for 40 min and aged at 700°C for 2000 h.

It was mentioned in Section 3.4. that the corrosion kinetics for the investigated Fe22Cr alloy follow the parabolic rate law [26,30]. It is also in agreement with the literature data collected for compositionally similar alloys, like Crofer 22 H or Crofer 22 APU [21,63,64]. These studies stated that following the parabolic rate law by the investigated alloys means that the outward Cr cation diffusion from the alloy particles to the oxide scale surface determines the corrosion phenomenon. Nevertheless, altering the grain and grain boundary diffusion fluxes by the pre-oxidation process seems to change the dominant character of the corrosion phenomenon, causing a slope change of the weight gain curve (Fig. 6C).

The increase of the slope to 0.69 for the pre-oxidized samples means that another competitive process influences the corrosion process. As the microstructural changes caused by the pre-oxidation, slow down the outward Cr cation diffusion process, the inward oxygen anion diffusion may play a relevant role for the corrosion phenomenon. However, the inward oxygen anion diffusion is described by the parabolic law of corrosion, as well as the outward chromium diffusion, so it cannot determine the increase of the weight gain curve's slope. On the other hand, Sabioni et al. investigated the relation between the oxidation growth rate of chromia scales and self-diffusion in Cr_2O_3 [59]. They revealed that the oxygen diffusion is faster than the chromium diffusion in chromia, both in the bulk and in the grain boundaries. Nevertheless, they confirmed that the calculations clearly indicate that neither bulk nor grain-boundary diffusion of oxygen can be responsible for the observed growth rate. To adequately elucidate the observed alteration in oxidation kinetics for the pre-oxidized porous alloy, further investigation is required.

The most crucial factor for lifespan prediction for porous alloys is the Cr reservoir inside the alloy`s particles. The lack of Cr in the alloy leads to breakaway corrosion formation. At SOC`s operating temperatures, the Cr level decrease is caused by two processes: Cr consumption for oxide scale (Cr_2O_3) formation and Cr evaporation [45]. Kim et al. investigated Cr volatilization of small (~25 μm) and large grain (~250 μm) Crofer 22 APU at 800°C for 700 h [50]. They revealed that the Cr evaporation rate for both samples is initially decreasing, but appears to stabilize at 400 h. The same behavior was observed by Stanislowski et al. for Crofer 22 APU [52,53]. However, the pre-oxidation process does not significantly impact the Cr evaporation rate for the porous Fe22Cr alloy, probably due to a lack of Mn, which precludes the formation of a protective spinel phase (see Fig. 7).

Based on the weight gain data (Fig. 6) it seems that the extension of the porous alloys` lifespan is possible for the pre-oxidized samples when compared with the raw porous alloys. Moreover, the pre-oxidation process performed at 900°C for 40 min leads to a reduction of the relative weight gain by ~5 times (Figure S.3) when compared with the reference samples. The same result was achieved by Tucker et al. for the P434L ferritic porous alloy pre-oxidized at 850°C for 10 h and further oxidized at 700°C for 500 h [41]. Hong et al. obtained ~3 times lower weight gain for pre-oxidized bulk T92 alloy at 700°C for 1 h at 21% N_2 and 79% O_2 atmosphere when compared with reference samples oxidized at 650°C [40].

An enhanced understanding of the pre-oxidation process's influence on the corrosion phenomenon is a complex issue. Taking into consideration the obtained results, it seems that a mix of parabolic and linear processes causes an increase of the weight gain curve slope. It was

confirmed that high temperature conditions do not only lead to oxide scale grain growth but also change the microstructure of the alloy, as was postulated in our previous work [42]. Therefore, for a detailed explanation of the pre-oxidation effect on the corrosion phenomenon in ferritic Cr-based alloys, further studies including 3D analysis of the pre-oxidized and oxidized samples are necessary. Based on the results presented in this work, the tomographic measurements of the porous alloy should be performed when the change of slope starts, for example as a part of synchrotron operando studies. In addition, the study of Cr and O diffusion coefficients in an oxide scale formed for pre-oxidized ferritic alloys should be performed by secondary ion mass spectrometry (SIMS) with the O^{18} isotope to determine the nature of the weight gain curve slope change that was observed in this study.

4. Conclusions

In this work, the impact of the pre-oxidation process on the corrosion properties of the porous ferritic Fe22Cr alloy was investigated. Based on possible applications of porous alloys as supports and interconnect elements in solid oxide cells, the aging temperature for this study was chosen to be 700°C and 750°C. For the pre-oxidation process, temperatures of 850°C and 900°C were chosen based on our previous study. The role pre-oxidation was evaluated by combining thermogravimetry, Cr evaporation measurements as well as SEM, TEM and synchrotron-based X-ray tomography analyses.

Weight gain measurements lasted up to 2000 h (plus the pre-oxidation process time) for the samples oxidized at 700°C. Although the values of weight gain after the pre-oxidation process were close between samples pre-oxidized at 850 °C (1.12%) and samples pre-oxidized at 900°C (1.05%), the achieved alloy's lifespan was different. After 2000 h, the alloy pre-oxidized at 850°C reached the threshold level for breakaway corrosion appearance, which is 6 wt%. For the samples pre-oxidized at 900 °C, the measured weight gain after 2000 h of oxidation at 700°C was significantly lower (3.91 wt%).

The conclusions from the SEM images were consistent with the weight gain data. For the samples pre-oxidized at 900°C and further oxidized at 700°C for 2000 h, there was no evidence for breakaway corrosion appearance. Regions of fully oxidized alloy were instead detected in samples pre-oxidized at 850°C and further oxidized at 700°C for 2000 h. Nevertheless, the SEM technique did not allow for evaluation of morphological changes after the pre-oxidation process.

For the detailed analysis of morphological and compositional changes in pre-oxidized porous alloys, X-ray tomography measurements were performed. The X-ray tomography study revealed that the oxide scale growth is not regular in the alloy's volume. After 5.5 h of oxidation at 850 °C, there were regions with only limited chromia growth. The difference between samples oxidized at 850°C for 3 h and oxidized at 850°C for 5.5 h was not significant in the context of oxide scale thickness or the oxidized regions. Nevertheless, after 30 h of oxidation at 850 °C, the oxide scale covered the alloy surface tightly. Moreover, oxide scale "paths," which connected some oxidized regions, were detected. It is in agreement with our previous study concerning the lifespan prediction of porous Fe22Cr at higher temperatures, like 850°C and 900°C.

The detailed analysis of the oxide scale grain size was achieved by TEM imaging. TEM images revealed that after the pre-oxidation step at 900°C for 40 min, the grain size of chromia cannot be easily determined for the oxide scale close to the alloy particle, while the size of chromia grains close to the air interface was 50 nm – 170 nm. On the other hand, the chromia grain size for the sample pre-oxidized at 900°C for 40 min and aged at 700°C for 2000 h was determined to be in range from 25 μm to 75 μm for chromia grains close to the alloy particle.

Cr evaporation measurements were performed for raw and pre-oxidized samples to observe if the process influenced the oxide scale growth rate. The analysis performed at 700°C for 500 h did not show any particular changes between raw and pre-oxidized samples. Thus, the pre-oxidation process might slow down the Cr^{3+} cation diffusion by

altering the grain and grain boundary diffusion fluxes, but it did not significantly influence Cr evaporation from the alloy particles.

Taking into consideration all analyses performed, the pre-oxidation process could extend the possible lifespan of the porous Fe22Cr alloy. The most important factor for this extension is the temperature of the process. The longest lifespan was achieved for samples pre-oxidized at 900°C for 40 min. The proficient use of the pre-oxidation process could extend the lifespan of the metallic component in the MS-SOCs and allow for more efficient operation of these devices at intermediate temperatures.

CRediT authorship contribution statement

Jan Froitzheim: Writing – review & editing, Resources, Investigation, Formal analysis. **Matthieu Tomas**: Writing – review & editing, Resources, Investigation. **Grzegorz Cempura**: Writing – review & editing, Validation, Investigation, Data curation. **Federica Marone**: Writing – review & editing, Software, Methodology. **Małgorzata Makowska**: Writing – original draft, Supervision, Formal analysis. **Damian Koszelow**: Writing – review & editing, Writing – original draft, Validation, Methodology, Investigation, Data curation, Conceptualization. **Sebastian Molin**: Writing – review & editing, Validation, Supervision, Resources, Conceptualization

Declaration of Competing Interest

The authors declare the following financial interests/personal relationships which may be considered as potential competing interests: Sebastian Molin reports financial support was provided by National Science Centre Poland. If there are other authors, they declare that they have no known competing financial interests or personal relationships that could have appeared to influence the work reported in this paper.

Data availability

Data will be made available on request.

Acknowledgments

Appendix A. Supporting information

Supplementary data associated with this article can be found in the online version at doi:10.1016/j.corsci.2024.112129.

References

[1] D.J. Young, High temperature oxidation and corrosion of metals, Elsevier, 2008.
[2] M.J. Pomeroy, Coatings for gas turbine materials and long term stability issues, Mater. Des. 26 (2005) 223–231, https://doi.org/10.1016/j.matdes.2004.02.005.
[3] H.J.C. Voorwald, R.C. Coisse, M.O.H. Cioffi, Fatigue strength of X45CrSi93 stainless steel applied as internal combustion engine valves, Procedia Eng. 10 (2011) 1256–1261, https://doi.org/10.1016/j.proeng.2011.04.209.
[4] B. Öztürk, A. Topcu, S. Öztürk, Ö.N. Cora, Oxidation, electrical and mechanical properties of Crofer®22 solid oxide fuel cell metallic interconnects manufactured through powder metallurgy, Int. J. Hydrog. Energy 43 (2018) 10822–10833, https://doi.org/10.1016/j.ijhydene.2018.01.078.
[5] A. Topcu, B. Öztürk, Ö.N. Cora, Performance evaluation of machined and powder metallurgically fabricated Crofer®22 APU interconnects for SOFC applications, Int.

J. Hydrog. Energy 47 (2022) 3437–3448, https://doi.org/10.1016/j.ijhydene.2021.06.036.

[6] J. Cao, M. Zheng, Z. Wang, X. Si, C. Li, X. Wang, Z. He, J. Qi, A low-temperature sealing method for metal-supported oxide fuel cell applications: Ni–Sn transient liquid phase bonding, Vacuum 187 (2021) 110048, https://doi.org/10.1016/j.vacuum.2021.110048.

[7] E. Zanchi, J. Ignaczak, B. Kamecki, P. Jasiński, S. Molin, A.R. Boccaccini, F. Smeacetto, Manganese–cobalt based spinel coatings processed by electrophoretic deposition method: the influence of sintering on degradation issues of solid oxide cell oxygen electrodes at 750∘c, Mater. (Basel) 14 (2021), https://doi.org/10.3390/ma14143836.

[8] F. D'Isanto, M. Salvo, S. Molin, D. Koszelow, H. Javed, S. Akram, A. Chrysanthou, F. Smeacetto, Glass-ceramic joining of Fe22Cr porous alloy to Crofer22APU: interfacial issues and mechanical properties, Ceram. Int. 48 (2022) 28519–28527, https://doi.org/10.1016/j.ceramint.2022.06.166.

[9] F. Smeacetto, M. Salvo, M. Ferraris, J. Cho, A.R. Boccaccini, Glass-ceramic seal to join Crofer 22 APU alloy to YSZ ceramic in planar SOFCs, J. Eur. Ceram. Soc. 28 (2008) 61–68, https://doi.org/10.1016/j.jeurceramsoc.2007.05.006.

[10] Z. Yang, Recent advances in metallic interconnects for solid oxide fuel cells, Int. Mater. Rev. 53 (2008) 39–52, https://doi.org/10.1179/174328007×212526.

[11] A.J. Abd Aziz, N.A. Baharuddin, M.R. Somalu, A. Muchtar, Review of composite cathodes for intermediate-temperature solid oxide fuel cell applications, Ceram. Int. 46 (2020) 23314–23325, https://doi.org/10.1016/j.ceramint.2020.06.176.

[12] M.C. Tucker, Progress in metal-supported solid oxide fuel cells: a review, J. Power Sources 195 (2010) 4570–4582, https://doi.org/10.1016/j.jpowsour.2010.02.035.

[13] B. Lemieszek, J. Ignaczak, B. Kamecki, J. Karczewski, M.B. Mogensen, S. Molin, P. Jasiński, Electrolytic deposition of reactive element thin films on Crofer 22 APU and evaluation of the resulting high-temperature corrosion protection properties at 700 °C–900 °C, Int. J. Hydrog. Energy (2022), https://doi.org/10.1016/j.ijhydene.2022.07.220.

[14] E. Zanchi, J. Ignaczak, S. Molin, G. Cempura, A.R. Boccaccini, F. Smeacetto, Electrophoretic co-deposition of Mn1.5Co1.5O4, Fe2O3 and CuO: unravelling the effect of simultaneous addition of Cu and Fe on the microstructural, thermo-mechanical and corrosion properties of in-situ modified spinel coatings for solid oxide cell intercon, J. Eur. Ceram. Soc. 42 (2022) 3271–3281, https://doi.org/10.1016/j.jeurceramsoc.2022.02.008.

[15] M. Palcut, L. Mikkelsen, K. Neufeld, M. Chen, R. Knibbe, P.V. Hendriksen, Corrosion stability of ferritic stainless steels for solid oxide electrolyser cell interconnects, Corros. Sci. 52 (2010) 3309–3320, https://doi.org/10.1016/j.corsci.2010.06.006.

[16] A. Holt, P. Kofstad, Electrical conductivity and defect structure of Cr2O3. II. Reduced temperatures (<~1000°C), Solid State Ionics. 69 (1994) 137–143. https://doi.org/10.1016/0167-2738(94)90402-2.

[17] P. Pavlasek, J. Rybař, S. Ďuriš, J. Palenčar, Effects of quartz glass insulation on platinum gold thermocouples, Meas. Sci. Rev. 19 (2019) 209–212, https://doi.org/10.2478/msr-2019-0027.

[18] H. Shahbaznejad, H. Ebrahimifar, A study on the oxidation and electrical behavior of crofer 22 APU solid oxide fuel cell interconnects with Ni-Co-CeO2 composite coating, J. Mater. Sci. Mater. Electron. 32 (2021) 7550–7566, https://doi.org/10.1007/s10854-021-05470-z.

[19] W.N. Liu, X. Sun, E. Stephens, M.A. Khaleel, Life prediction of coated and uncoated metallic interconnect for solid oxide fuel cell applications, J. Power Sources 189 (2009) 1044–1050, https://doi.org/10.1016/j.jpowsour.2008.12.143.

[20] B. Timurkutluk, S. Toros, S. Onbilgin, H.G. Korkmaz, Determination of formability characteristics of Crofer 22 APU sheets as interconnector for solid oxide fuel cells, Int. J. Hydrog. Energy 43 (2018) 14638–14647, https://doi.org/10.1016/j.ijhydene.2018.04.243.

[21] N.J. Magdefrau, L. Chen, E.Y. Sun, M. Aindow, Effects of alloy heat treatment on oxidation kinetics and scale morphology for Crofer 22 APU, J. Power Sources 241 (2013) 756–767, https://doi.org/10.1016/j.jpowsour.2013.03.181.

[22] R.N. Hajra, H. Tripathy, C. Sudha, N. Vijayashanthi, S. Raju, S. Saroja, Effect of sigma phase on thermophysical properties of Fe55Cr45 alloy, Intermetallics 112 (2019) 106552, https://doi.org/10.1016/j.intermet.2019.106552.

[23] K. Popova, T. Prošek, Corrosion monitoring in atmospheric conditions: a review, Met. (Basel) 12 (2022), https://doi.org/10.3390/met12020171.

[24] H. Simillion, O. Dolgikh, H. Terryn, J. Deconinck, Atmospheric corrosion modeling, Corros. Rev. 32 (2014) 73–100, https://doi.org/10.1515/corrrev-2014-0023.

[25] Y. Cai, Y. Xu, Y. Zhao, X. Ma, Atmospheric corrosion prediction: a review, Corros. Rev. 38 (2020) 299–321, https://doi.org/10.1515/corrrev-2019-0100.

[26] D. Koszelow, M. Makowska, A. Drewniak, G. Cempura, P. Jasiński, S. Molin, High-temperature Corrosion of ∼ 30 Pct Porous FeCr stainless steels in air: long-term evaluation up to breakaway, Metall. Mater. Trans. A Phys. Metall. Mater. Sci. (2023), https://doi.org/10.1007/s11661-023-07005-z.

[27] E. Sarasketa-Zabala, L. Otaegi, L.M. Rodriguez-Martinez, M.A. Alvarez, N. Burgos, F. Castro, I. Villarreal, High temperature stability of porous metal substrates under highly humidified hydrogen conditions for metal supported Solid Oxide Fuel Cells, Solid State Ion. 222–223 (2012) 16–22, https://doi.org/10.1016/j.ssi.2012.06.014.

[28] J.A. Glasscock, L. Mikkelsen, Å.H. Persson, G. Pećanac, J. Malzbender, P. Blennow, F. Bozza, P.V. Hendriksen, Porous Fe21Cr7Al1Mo0.5Y metal supports for oxygen transport membranes: thermo-mechanical properties, sintering and corrosion behaviour, Solid State Ion. 242 (2013) 33–44, https://doi.org/10.1016/j.ssi.2013.04.006.

[29] D. Koszelow, M. Makowska, F. Marone, J. Karczewski, P. Jasiński, S. Molin, High temperature corrosion evaluation and lifetime prediction of porous Fe22Cr

[30] D. Koszelow, M. Makowska, F. Marone, J. Karczewski, P. Jasiński, S. Molin, High Temperature Corrosion Evaluation and Lifetime Prediction of Porous Fe22Cr Stainless Steel in Air in Temperature Range 700-900°C, Corros. Sci. 189 (2021) 109589, https://doi.org/10.1016/j.corsci.2021.109589.

[31] J. Karczewski, K.J. Dunst, P. Jasinski, S. Molin, High temperature corrosion and corrosion protection of porous Ni22Cr alloys, Surf. Coat. Technol. 261 (2015) 385–390, https://doi.org/10.1016/j.surfcoat.2014.10.051.

[32] S. Molin, B. Kusz, M. Gazda, P. Jasinski, Evaluation of porous 430L stainless steel for SOFC operation at intermediate temperatures, J. Power Sources 181 (2008) 31–37, https://doi.org/10.1016/j.jpowsour.2007.10.009.

[33] M.C. Tucker, Progress in metal-supported solid oxide electrolysis cells: a review, Int. J. Hydrog. Energy 45 (2020) 24203–24218, https://doi.org/10.1016/j.ijhydene.2020.06.300.

[34] E. Stefan, C. Denonville, Y. Larring, M. Stange, R. Haugsrud, Oxidation study of porous metal substrates for metal supported proton ceramic electrolyzer cells, Corros. Sci. 164 (2020) 108335, https://doi.org/10.1016/j.corsci.2019.108335.

[35] P. Huczkowski, N. Christiansen, V. Shemet, J. Piron-Abellan, L. Singheiser, W.J. Quadakkers, Oxidation induced lifetime limits of chromia forming ferritic interconnector steels, J. Fuel Cell Sci. Technol. 1 (2004) 30, https://doi.org/10.1115/1.1782925.

[36] P. Huczkowski, V. Shemet, J. Piron-Abellan, L. Singheiser, W.J. Quadakkers, N. Christiansen, Oxidation limited life times of chromia forming ferritic steels, Mater. Corros. 55 (2004) 825–830, https://doi.org/10.1002/maco.200303798.

[37] M. Palcut, L. Mikkelsen, K. Neufeld, M. Chen, R. Knibbe, P.V. Hendriksen, Improved oxidation resistance of ferritic steels with LSM coating for high temperature electrochemical applications, Int. J. Hydrog. Energy 37 (2012) 8087–8094, https://doi.org/10.1016/j.ijhydene.2011.11.138.

[38] M. Palcut, L. Mikkelsen, K. Neufeld, M. Chen, R. Knibbe, P.V. Hendriksen, Corrosion stability of ferritic stainless steels for solid oxide electrolyser cell interconnects, Corros. Sci. 52 (2010) 3309–3320.

[39] B. Talic, S. Molin, P.V. Hendriksen, H.L. Lein, Effect of pre-oxidation on the oxidation resistance of Crofer 22 APU, Corros. Sci. 138 (2018) 189–199, https://doi.org/10.1016/j.corsci.2018.04.016.

[40] H. Xu, Z. Liang, J. DIng, Q. Zhao, S. Guan, Effect of pre-oxidation on the steam oxidation of heat-resistant steel T92, High. Temp. Mater. Process. 37 (2018) 733–739, https://doi.org/10.1515/htmp-2017-0037.

[41] F. Shen, M.M. Welander, M.C. Tucker, Oxidation of porous stainless steel supports for metal-supported solid oxide electrolysis cells, Int. J. Hydrog. Energy 48 (2023) 12168–12175, https://doi.org/10.1016/j.ijhydene.2022.11.235.

[42] D. Koszelow, S. Molin, J. Karczewski, F. Marone, M. Makowska, Morphology changes in Fe-Cr porous alloys upon high-temperature oxidation quantified by X-ray tomographic microscopy, Mater. Des. 215 (2022) 110492, https://doi.org/10.1016/j.matdes.2022.110492.

[43] J. Froitzheim, H. Ravash, E. Larsson, L.G. Johansson, J.E. Svensson, Investigation of Chromium Volatilization from FeCr Interconnects by a Denuder Technique, J. Electrochem. Soc. 157 (2010) B1295, https://doi.org/10.1149/1.3462987.

[44] D. Paganin, S.C. Mayo, T.E. Gureyev, P.R. Miller, S.W. Wilkins, Simultaneous phase and amplitude extraction from a single defocused image of a homogeneous object, J. Microsc. 206 (2002) 33–40, https://doi.org/10.1046/j.1365-2818.2002.01010.x.

[45] H. Falk-Windisch, J.E. Svensson, J. Froitzheim, The effect of temperature on chromium vaporization and oxide scale growth on interconnect steels for Solid Oxide Fuel Cells, J. Power Sources 287 (2015) 25–35, https://doi.org/10.1016/j.jpowsour.2015.04.040.

[46] E. Stefan, C. Denonville, Y. Larring, M. Stange, R. Haugsrud, Oxidation study of porous metal substrates for metal supported proton ceramic electrolyzer cells, Corros. Sci. 164 (2020) 108335, https://doi.org/10.1016/j.corsci.2019.108335.

[47] H. Falk-Windisch, J.E. Svensson, J. Froitzheim, The effect of temperature on chromium vaporization and oxide scale growth on interconnect steels for Solid Oxide Fuel Cells, J. Power Sources 287 (2015) 25–35, https://doi.org/10.1016/j.jpowsour.2015.04.040.

[48] C. Goebel, R. Berger, C. Bernuy-Lopez, J. Westlinder, J.E. Svensson, J. Froitzheim, Long-term (4 year) degradation behavior of coated stainless steel 441 used for solid oxide fuel cell interconnect applications, J. Power Sources 449 (2020), https://doi.org/10.1016/j.jpowsour.2019.227480.

[49] R. Sachitanand, M. Sattari, J.E. Svensson, J. Froitzheim, Evaluation of the oxidation and Cr evaporation properties of selected FeCr alloys used as SOFC interconnects, Int. J. Hydrog. Energy 38 (2013) 15328–15334, https://doi.org/10.1016/j.ijhydene.2013.09.044.

[50] B.K. Kim, Y.S. Ko, I.H. Jung, H.N. Han, K.W. Yi, D.I. Kim, Role of the alloy grain boundaries in the high-temperature oxidation and Cr volatilization of 22wt% Cr ferritic stainless steel for SOFC applications, Corros. Sci. 213 (2023) 110940, https://doi.org/10.1016/j.corsci.2022.110940.

[51] M. Reisert, V. Berova, A. Aphale, P. Singh, M.C. Tucker, Oxidation of porous stainless steel supports for metal-supported solid oxide fuel cells, Int. J. Hydrog. Energy 45 (2020) 30882–30897, https://doi.org/10.1016/j.ijhydene.2020.08.015.

[52] M. Stanislowski, E. Wessel, K. Hilpert, T. Markus, L. Singheiser, Chromium Vaporization from High-Temperature Alloys, J. Electrochem. Soc. 154 (2007) A295, https://doi.org/10.1149/1.2434690.

[53] M. Stanislowski, J. Froitzheim, L. Niewolak, W.J. Quadakkers, K. Hilpert, T. Markus, L. Singheiser, Reduction of chromium vaporization from SOFC interconnectors by highly effective coatings, J. Power Sources 164 (2007) 578–589, https://doi.org/10.1016/j.jpowsour.2006.08.013.

[54] A.C.S. Sabioni, J.N.V. Souza, V. Ji, F. Jomard, V.B. Trindade, J.F. Carneiro, Study of ion diffusion in oxidation films grown on a model Fe-15%Cr alloy, Solid State Ion. 276 (2015) 1–8, https://doi.org/10.1016/j.ssi.2015.03.027.

[55] P. Kofstad, K.P. Lillerud, Chromium transport through Cr2O3 scales I. On lattice diffusion of chromium, Oxid. Met. 17 (1982) 177–194, https://doi.org/10.1007/BF00738381.

[56] P. Kofstad, Defects and transport properties of metal oxides, Oxid. Met. 44 (1995) 3–27, https://doi.org/10.1007/BF01046721.

[57] R.E. Lobnig, H.P. Schmidt, K. Hennesen, H.J. Grabke, Diffusion of cations in chromia layers grown on iron-base alloys, Oxid. Met. 37 (1992) 81–93, https://doi.org/10.1007/BF00665632.

[58] A.C.S. Sabioni, B. Lesage, A.M. Huntz, J.C. Pivin, C. Monty, Self-diffusion in Cr2O3 I. Chromium diffusion in single crystals, Philos. Mag. A Phys. Condens. Matter, Struct. Defects Mech. Prop. 66 (1992) 333–350, https://doi.org/10.1080/01418619208201560.

[59] A.C.S. Sabioni, A.M. Huntz, J. Philibert, B. Lesage, C. Monty, Relation between the oxidation growth rate of chromia scales and self-diffusion in Cr2O3, J. Mater. Sci. 27 (1992) 4782–4790, https://doi.org/10.1007/BF01166020.

[60] R.K. Gupta, R.K.S. Raman, C.C. Koch, B.S. Murty, Effect of nanocrystalline structure on the corrosion of a Fe20Cr alloy, Int. J. Electrochem. Sci. 8 (2013) 6791–6806, https://doi.org/10.1016/s1452-3981(23)14806-1.

[61] T. Suzuoka, Lattice and Grain Boundary in Polycrystals, Trans. Jim. 2 (1961).

[62] S.C. Tsai, A.M. Huntz, C. Dolin, Growth mechanism of Cr2O3 scales: oxygen and chromium diffusion, oxidation kinetics and effect of yttrium, Mater. Sci. Eng. A. 212 (1996) 6–13, https://doi.org/10.1016/0921-5093(96)10173-8.

[63] A.W.B. Skilbred, R. Haugsrud, Sandvik Sanergy HT - A potential interconnect material for LaNbO 4-based proton ceramic fuel cells, J. Power Sources 206 (2012) 70–76, https://doi.org/10.1016/j.jpowsour.2012.01.101.

[64] B. Talic, S. Molin, P.V. Hendriksen, H.L. Lein, Effect of pre-oxidation on the oxidation resistance of Crofer 22 APU, Corros. Sci. 138 (2018) 189–199, https://doi.org/10.1016/j.corsci.2018.04.016.